Quadrature squeezing of 10math xmlns="http://www.w3.org/1998/Math/MathML">msup>mrow>/mrow>mn>4/mn>/msup>/math> spatial modes via manipulation of diffraction

Lida Zhang (□□□), Vincent Boyer, and M. O. Scully

Phys. Rev. A **105**, 023725 — Published 28 February 2022

DOI: 10.1103/PhysRevA.105.023725

Quadrature Squeezing of 10^4 Spatial Modes via Manipulation of Diffraction

Lida Zhang (张理达)[1],* Vincent Boyer[5], and M. O. Scully[1,3,4]
[1] *Texas A & M University, College Station, Texas 77843, USA*
[2] *Department of Physics and Astronomy, Texas A & M University, College Station, Texas 77843, USA*
[3] *Baylor University, Waco, Texas 76798, USA*
[4] *Princeton University, Princeton, NJ 08544, USA and*
[5] *Midlands Ultracold Atom Research Centre, School of Physics and Astronomy, University of Birmingham, Edgbaston, Birmingham B15 2TT, UK*
(Dated: February 14, 2022)

We propose a general and feasible approach to realize a large number of squeezed spatial modes. This is achieved by manipulation of paraxial diffraction such that the critical wave components with most significant squeezing contribute in-phase to the spatial squeezing. As an example, we then demonstrate that it is possible to achieve localized squeezing of ~ -1.51 dB at an area $10^2\ \mu m^2$ within a homogeneously squeezed spatial regime of $w_p = 1\ mm^2$ using four-wave mixing (FWM) based on current experimental settings, corresponding to approximately 10^4 squeezed spatial modes, which is $> 10^2$ larger in number of squeezed modes and also ~ 6 times stronger in squeezing as compared to that obtained in the state-of-the-art experiment. We also show that the obtained extremely localized squeezed light can be directly applied to enhance the signal-to-noise ratio in quantum imaging of weakly absorbing objects by a factor of ~ 3.5 at a spatial resolution of $d \sim 1\ mm$ where d is the detector size.

I. INTRODUCTION

Light can have different modes and quantum states simultaneously. Owing to this intrinsic dual nature, it is possible to realize multimode quantum light, e.g., multimode entanglement and quadrature squeezing in the discrete-variable and continuous-variable (CV) regime respectively [1]. Owing to the intrinsic insensitivity to environmental decoherence and the striking possibility of substantial scalability [2], multimode quantum light highlights its unparalleled advantages in quantum information processing. In particular, in the CV regime multimode quadrature squeezing has been revealed to be capable of achieving enhanced precision in quantum measurements [3, 4], and generating CV cluster states [5, 6] that hold promise for one-way quantum computation [7–11].

Substantial progresses have been made to achieve up to squeezing of 10^6 modes in the time domain [12, 13], however, simultaneous squeezing of many spatial modes, i.e., multi-spatial-mode (MSM) squeezing has been lacking. Squeezing of a few spatial modes can be generated via different physical mechanisms, e.g, the $\chi^{(2)}$ processes including parametric down-conversion or optical parametric amplification [14–17]. A highly flexible scheme is the conjugate four-wave mixing (FWM) [18–28], a $\chi^{(3)}$ process in which the linear and nonlinear responses of the medium can be easily tailored by the applied laser fields [18–24]. Based on FWM, the most recent record is the simultaneous squeezing of ~ 75 spatial modes in a single laser beam in the state-of-the-art experiment [23], in which a squeezing of ~ -0.25 dB is obtained in a minimal area of $\sim 180^2\ \mu m^2$. MSM squeezing in a single laser beam as a multimode quantum light source does not only show advantages in quantum communication in terms of the complexity of protocols [9, 29], but can as well be of great importance to diverse applications where either MSM or few-spatial-mode squeezing is required to enhance spatial resolution, e.g., in quantum imaging [3], measurements of nanometer displacement [30, 31] and biological systems [32, 33] since the single MSM squeezed laser beam can be decomposed to a few spatial modes with much stronger squeezing defined by the mode of the local oscillator [23].

A large number of squeezed spatial modes within a single finite-size laser beam suggests extremely localized spatial squeezing. Paraxial diffraction is believed to be the key obstacle to achieve strongly localized squeezing, since it imposes phase shifts to affect the angle of the squeezing ellipse differently for the various transverse spatial wave components which might contribute out-of-phase to the spatial squeezing. A seemingly straightforward way to achieve simultaneous squeezing of many localized spatial modes would be to eliminate the paraxial diffraction, by exploring physical mechanisms including nonlocal linear response due to atomic motion [34, 35], coherent population trapping [36, 37] and optically written waveguide [38]. These schemes to eliminate diffraction usually cancel only the propagation-accumulated phase shifts for small paraxial wave components $|\boldsymbol{k}_\perp| \sim 1/w_p$ ($\boldsymbol{k}_\perp$ is the transverse wavevector of the component, and w_p is the probe beam waist) since the larger transverse wave components $|\boldsymbol{k}_\perp| \gg 1/w_p$ are negligible for the intensity profile. However, the larger components $|\boldsymbol{k}_\perp|$ are crucially important for squeezing in an area $\ll w_p^2$ and may contribute out-of-phase to the spatial squeezing. Thus in order to achieve extremely localized squeezing, it is required to eliminate the phase shifts for large $|\boldsymbol{k}_\perp|$. In typical $\chi^{(2)}$ or $\chi^{(3)}$ media, the nonlinearity is limited and can not support the cancellation of

* zhanglida@gmail.com

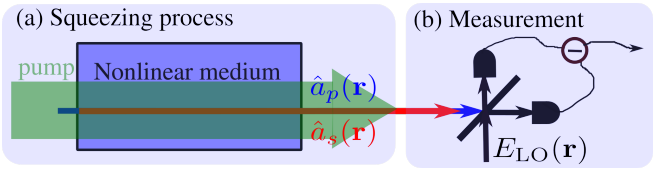

FIG. 1. (Color online) (a) A schematic illustration of the squeezing process. The nonlinear medium is driving by a pump field to generated MSM squeezed probe and single fields denoted by $\hat{a}_p(\boldsymbol{r})$ and $\hat{a}_s(\boldsymbol{r})$ respectively. (b) The MSM squeezing is measured by a bichromatic homodyne detection method in which the local oscillator $E_{\rm LO}(\boldsymbol{r})$ consists of two strong laser beams with frequencies equal to that of $\hat{a}_p(\boldsymbol{r})$ and $\hat{a}_s(\boldsymbol{r})$. The MSM squeezing is detected by varying the spatial size of $E_{\rm LO}(\boldsymbol{r})$.

phase shifts for large $|\boldsymbol{k}_\perp|$, thus it is physically impractical to achieve extremely localized squeezing via reduction of diffraction.

Alternatively, here we propose a general and feasible approach to realize strong squeezing at an area A ($\lambda^2 \ll A \ll w_p^2$ with λ being the laser wavelength) in a finite-size probe beam, which is achieved surprisingly via not elimination but manipulation of diffraction. The central idea is to focus on the critical wave components which contribute most significantly to the spatial squeezing. By analyzing the squeezing properties of these critical wave components, we are able to identify the conditions for the susceptibilities to control the diffraction such that all wave components contribute constructively to the spatial squeezing. These conditions can be easily satisfied by changing the laser parameters like detunings and intensities. Since the analysis is derived from the paraxial propagation equation of the quantum fields, therefore it does not depend on the actual squeezing process. In other words, our theory is applicable to either the $\chi^{(2)}$ or $\chi^{(3)}$ nonlinear processes. As an example, we apply our theory to the FWM and show that it is possible to reach quadrature squeezing of -1.51 dB at an area of 10^2 μm^2 for a probe beam with size ~ 1 mm^2 in realistic parameter regime, corresponding to around 10^4 detectable squeezed spatial modes.

II. THEORETICAL MODEL

Considering a general squeezing process depicted in Fig. 1(a), the propagation equations for the two quantum fields in the continuous-wave limit are given by

$$\left(\frac{d}{dz}+\frac{i}{2k_p}\nabla_\perp^2\right)\hat{a}_p^\dagger(\boldsymbol{r}_\perp,z)=-i\hat{P}_p^\dagger(\boldsymbol{r})\,, \tag{1a}$$

$$\left(\frac{d}{dz}-\frac{i}{2k_s}\nabla_\perp^2\right)\hat{a}_s(\boldsymbol{r}_\perp,z)=i\hat{P}_s(\boldsymbol{r}) \tag{1b}$$

where $\hat{a}_p(\boldsymbol{r}_\perp,z)$ $[\hat{a}_s(\boldsymbol{r}_\perp,z)]$ is the annihilation operator for the quantum probe [signal] field with associated wavenumber k_p $[k_s]$, $\hat{P}_p$ $[\hat{P}_s]$ represents the corresponding polarization operator of the nonlinear medium. The terms including $\nabla_\perp^2$ introduces the paraxial diffraction which affects both the squeezing degree and ellipse angles for different $\boldsymbol{k}_\perp$. Eqs. (1) serve as a general description of spatial squeezing in a traveling-wave setting and can thus be applied to different mechanisms such as the $\chi^{(2)}$ or $\chi^{(3)}$ nonlinear process.

A general form for $\hat{P}_j(\boldsymbol{r})$ in the squeezing process can be written as a linear combination of the field operators

$$\hat{P}_p^\dagger(\boldsymbol{r})=C_p\chi_{pp}\hat{a}_p^\dagger(\boldsymbol{r})+C_p\chi_{sp}\hat{a}_s(\boldsymbol{r})+\hat{F}_p(\boldsymbol{r})\,, \tag{2a}$$

$$\hat{P}_s(\boldsymbol{r})=C_s\chi_{ps}\hat{a}_p^\dagger(\boldsymbol{r})+C_s\chi_{ss}\hat{a}_s(\boldsymbol{r})+\hat{F}_s(\boldsymbol{r})\,, \tag{2b}$$

C_p $[C_s]$ is a dimensional constant for the probe [signal] field. χ_{ij} with $i,j\in\{p,s\}$ describes respectively the linear and nonlinear susceptibilities of the medium whose exact expressions are usually complicated depending on the medium properties and laser parameters. $\hat{F}_p(\boldsymbol{r})$ and $\hat{F}_s(\boldsymbol{r})$ denote the quantum noises for the two fields respectively owing to dissipative and dephasing processes in the nonlinear medium. In principle, χ_{ij} should also be position-dependent determined by the specific physical process. However, in order to focus on the diffraction of the quantum fields themselves, we assume χ_{ij} to be spatially homogeneous for the two quantum fields. This is possible when the pump lasers driving the squeezing process are spatially much broader and also much brighter (low-depletion regime) than the two quantum fields.

Inserting Eqs. (2) into Eqs. (1) and Fourier transforming them from position to momentum space leads to

$$\frac{d}{d\zeta}\hat{\boldsymbol{a}}(\boldsymbol{k}_\perp,\zeta)=i\hat{H}(\boldsymbol{k}_\perp)\hat{\boldsymbol{a}}(\boldsymbol{k}_\perp,\zeta)+\hat{\boldsymbol{f}}(\boldsymbol{k}_\perp,\zeta) \tag{3}$$

where $\hat{\boldsymbol{a}}(\boldsymbol{k}_\perp,\zeta)=\{\hat{a}_p^\dagger(-\boldsymbol{k}_\perp,\zeta),\hat{a}_s(\boldsymbol{k}_\perp,\zeta)\}^T$ with $\hat{a}_j(\boldsymbol{k}_\perp,\zeta)=(\sqrt{2\pi})^{-2}\iint_{-\infty}^{\infty}\hat{a}_j(\boldsymbol{r}_\perp,\zeta)e^{-i\boldsymbol{k}_\perp\cdot\boldsymbol{\xi}}d\boldsymbol{\xi}$ for $j\in\{p,s\}$. Here we have introduced the dimensionless variables $\boldsymbol{\xi}=\boldsymbol{r}_\perp/w_p$, $\zeta=z/S_z$ and $S_z=k_pw_p^2$ with w_p and S_z being the transverse and propagation scales respectively. $\hat{H}(\boldsymbol{k}_\perp)$ is given by

$$H=\begin{bmatrix}-\chi_{pl}+\frac{k_\perp^2}{2} & -\chi_{pn}\\ \chi_{sn} & \chi_{sl}-\frac{k_\perp^2}{2}\end{bmatrix}, \tag{4}$$

where $k_\perp^2=k_x^2+k_y^2$, $\chi_{pl}=C_pS_z\chi_{pp}$ and similarly for χ_{pn}, χ_{sl} and χ_{sn}. Furthermore $\hat{\boldsymbol{f}}(\boldsymbol{k}_\perp,\zeta)=\{\hat{f}_p(\boldsymbol{k}_\perp,\zeta),\hat{f}_s(\boldsymbol{k}_\perp,\zeta)\}^T=S_z\{\hat{F}_p(\boldsymbol{k}_\perp,\zeta),\hat{F}_s(\boldsymbol{k}_\perp,\zeta)\}^T$. In the experiments that have been done to demonstrate squeezing, the laser parameters are usually chosen to work in the dispersive regime where $|\mathrm{Im}[\chi_j]|\ll|\mathrm{Re}[\chi_j]|$ $(j\in\{pl,sl,pn,sn\})$ such that the quantum noises which are detrimental to the squeezing can be minimized. We may thus assume χ_j to be real and neglect the noise terms in the following. A general analysis of the noise properties in the context of FWM process is given in the Appendix C.

The effective Hamiltonian for Eq. (3) can be written as

$$\begin{aligned}\hat{H}_{\text{eff}} =&(\chi_{pl} - \frac{k_\perp^2}{2})\hat{a}_p^\dagger(-\boldsymbol{k}_\perp)\hat{a}_p(-\boldsymbol{k}_\perp)\\ &+ (\chi_{sl} - \frac{k_\perp^2}{2})\hat{a}_s(\boldsymbol{k}_\perp)\hat{a}_s(\boldsymbol{k}_\perp)\\ &+ \chi_{pn}\hat{a}_p(-\boldsymbol{k}_\perp)\hat{a}_s(\boldsymbol{k}_\perp) + \chi_{sn}\hat{a}_p^\dagger(-\boldsymbol{k}_\perp)\hat{a}_s^\dagger(\boldsymbol{k}_\perp) \quad (5)\end{aligned}$$

based on which Eq. (3) can be obtained from $\frac{\partial}{\partial\zeta}\hat{a} = i[\hat{H}_{\text{eff}}, \hat{a}] + \hat{f}_j$. The last two terms in the effective Hamiltonian describe a typical squeezing process, thus quadrature squeezing will be generated between the wave component $\hat{a}_p(-\boldsymbol{k}_\perp)$ and $\hat{a}_s(\boldsymbol{k}_\perp)$. Meanwhile, the squeezing process is controlled by the paraxial diffraction term $k_\perp^2$ in the sense that both the squeezing degree and angle would be varied considerably as $k_\perp$ changes. For a given spatial mode, the corresponding squeezing degree is determined by a weighted summation over squeezing of all wave components where the weighting function is given by the momentum spectrum of this spatial mode. Depending on the squeezing ellipse orientations, each wave component may contribute in-phase or out-of-phase to the spatial squeezing. Thus the spatial squeezing will be significantly affected by the diffraction. Fortunately, the effect of the diffraction can be controlled by the susceptibilities χ_j. If we are able to manipulate χ_j by tuning the laser parameters such that the most significantly squeezed wave components have their squeezing ellipses oriented in the same direction, then they will contribute in-phase to the spatial squeezing. Note that this does not necessarily mean that the paraxial diffraction needs to be eliminated.

III. MANIPULATION OF DIFFRACTION

Having established that the diffraction is the key factor limiting the number of squeezed spatial modes, here we discuss how to control the diffraction by exploiting the intrinsic properties of the squeezing process itself. We first write the formal solution to Eq. (3)

$$\hat{\boldsymbol{a}}(\boldsymbol{k}_\perp, \zeta) = M(\boldsymbol{k}_\perp, \zeta)\hat{\boldsymbol{a}}(\boldsymbol{k}_\perp, 0) \quad (6)$$

where $M(\boldsymbol{k}_\perp, \zeta) = e^{iH(\boldsymbol{k}_\perp)\zeta}$, and the eigenvalues of $H(\boldsymbol{k}_\perp)$ are

$$\beta_{1,2} = \frac{\Delta\chi_l}{2} \pm i\beta \quad (7)$$

with $\beta = \sqrt{\chi_{pn}\chi_{sn} - (\chi_l - k_\perp^2)^2/4}$, $\Delta\chi_l = \chi_{sl} - \chi_{pl}$ and $\chi_l = \chi_{sl} + \chi_{pl}$ being the difference and sum of the two linear atomic susceptibilities respectively. Then we have

$$M(\boldsymbol{k}_\perp, \zeta) = \begin{bmatrix} \cosh\beta\zeta + \frac{i\delta}{2\beta}\sinh\beta\zeta & -\frac{i\chi_{pn}}{\beta}\sinh\beta\zeta \\ \frac{i\chi_{sn}}{\beta}\sinh\beta\zeta & \cosh\beta\zeta - \frac{i\delta}{2\beta}\sinh\beta\zeta \end{bmatrix} \quad (8)$$

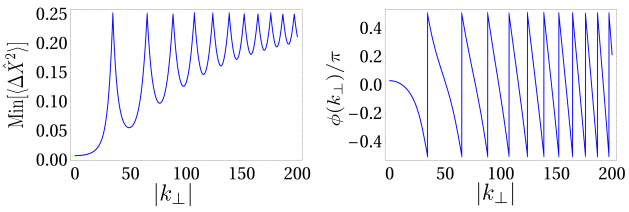

FIG. 2. (Color online) The minimum variance and ellipse angle as a function of $|k_\perp|$. Here we have taken the linear and nonlinear susceptibilities from the FWM example considered in Fig. 3. Parameters are the same as in the caption of Fig. 3 except $\Delta = 16.4\Gamma_{32}$.

with $\delta = k_\perp^2 - \chi_l$, and we have neglected the common phase term $e^{i\Delta\chi_l\zeta/2}$ which is not important here. The commutation relation $[\hat{a}_j(\boldsymbol{k}_\perp, \zeta), \hat{a}_j^\dagger(\boldsymbol{k}_\perp', \zeta)] = \delta(\boldsymbol{k}_\perp - \boldsymbol{k}_\perp')$ requires $\chi_{sn} = \chi_{pn}$ which is usually the case in the experiments, we thus set $\chi_{pn} = \chi_{sn} = \chi_{nl}$.

We then analyze the squeezing properties of each spatial wave component $\boldsymbol{k}_\perp$, the corresponding quadrature operator is given by $\hat{X}(\boldsymbol{k}_\perp, \zeta, \theta) = \{i[\hat{a}_p(-\boldsymbol{k}_\perp, \zeta) + \hat{a}_s(\boldsymbol{k}_\perp, \zeta)]e^{-i\theta} + h.c.\}/(2\sqrt{2})$. The variation for $\hat{X}(\boldsymbol{k}_\perp, \zeta, \theta)$ is

$$\begin{aligned}&\langle\Delta\hat{X}^2(\boldsymbol{k}_\perp, \zeta, \theta)\rangle\\ &= \frac{1}{4}\left[1 + 2C^2 - 2C\sqrt{1+C^2}\cos(\phi(\boldsymbol{k}_\perp) - 2\theta)\right] \quad (9a)\\ &\phi(\boldsymbol{k}_\perp) = \arctan\left[\frac{2\beta\cosh(\beta\zeta)}{(k_\perp^2 - \chi_l)\sinh(\beta\zeta)}\right] \quad (9b)\end{aligned}$$

with $C = \chi_{nl}\sinh(\beta\zeta)/\beta$. It can be seen that β plays the central role determining both the variance $\langle\Delta\hat{X}^2\rangle$ and phase ϕ. β is very sensitive to $\boldsymbol{k}_\perp$ due to the quadratic dependence, and becomes purely imaginary for large $|\boldsymbol{k}_\perp|$ ($k_\perp^2 \geq \text{Max}[\chi_l + 2|\chi_{nl}|, 0]$) where both the squeezing degree and phase undergo increasingly rapid oscillations.

The spatial squeezing in a certain area can be then obtained by taking into account the contributions from the spatial components. Maximal spatial squeezing can be obtained by considering a local oscillator in which the phase of each spatial component is controlled to minimize $\langle\Delta\hat{X}^2(\boldsymbol{k}_\perp, \zeta, \theta)\rangle$ in Eq. (9a). Obviously, preparing such a local oscillator would be very challenging. Instead, we consider the situation that the phase of each component in the local oscillator is constant, and this constant phase will be denoted as θ. We would like now to find the optimal choice for θ to achieve extremely localized spatial squeezing.

Extremely localized spatial squeezing will crucially depends on the squeezing properties of large $|\boldsymbol{k}_\perp|$ for which β will become purely imaginary. For large $|\boldsymbol{k}_\perp|$, β turns from real to purely imaginary such that C will oscillate periodically as $k_\perp$ grows. As a result, the variance $\langle\Delta\hat{X}^2\rangle$ changes periodically. We then find that for $\chi_{nl} > 0$ and $\theta = 0$ there is a minimal $\langle\Delta\hat{X}^2\rangle$ in each period when

$|\beta|\zeta = (n+1/2)\pi$ at which $\phi(\boldsymbol{k}_\perp) = 0$ [see Eq. (9) and also Fig. 2]. For $\chi_{nl} < 0$, $\theta = \pi/2$ has to be chosen to have a minimal $\langle \Delta\hat{X}^2 \rangle$ in each period. We call these wave components having minimal $\langle \Delta\hat{X}^2 \rangle$ as "critical wave components" since they exhibit strongest squeezing in each period.

Based on the previous discussions, the optimal choice for the phase of the local oscillator to maximize the localized spatial squeezing would be either $\theta = 0$ or $\theta = \pi/2$ such that the critical wave components contribute constructively. In order to have in-phase contributions from all wave components, one would require $\langle \Delta\hat{X}^2(\boldsymbol{k}_\perp, \zeta_L) \rangle \leq 1/4$ for either $\theta = 0$ or $\theta = \pi/2$, i.e.,

$$\frac{\chi_{nl}(\chi_l - k_\perp^2 + 2\chi_{nl}) \sinh^2(\beta\zeta_L)}{\beta^2} \leq 0 \quad \text{for } \theta = 0 \tag{10a}$$

$$\frac{\chi_{nl}(k_\perp^2 - \chi_l + 2\chi_{nl}) \sinh^2(\beta\zeta_L)}{\beta^2} \leq 0 \quad \text{for } \theta = \frac{\pi}{2} \tag{10b}$$

here $\zeta_L = L/S_z$ with L being the interaction length of the FWM process. Satisfying this condition for all $\boldsymbol{k}_\perp$ then leads to

$$\chi_{nl} > 0, \chi_l \leq -2\chi_{nl} \quad \text{for } \theta = 0 \tag{11a}$$

$$\chi_{nl} < 0, \chi_l \leq 2\chi_{nl} \quad \text{for } \theta = \frac{\pi}{2} \tag{11b}$$

Eqs. (11) also indicates that β will be imaginary for all $\boldsymbol{k}_\perp$, i.e., there is no exponential growth of squeezing for any $\boldsymbol{k}_\perp$. This is in sharp contrast to the single-mode case in which strongest squeezing is obtained for real β because of exponential growth. It is also worthy noting here that satisfying Eqs. (11) may break the phase-matching condition for different $\boldsymbol{k}_\perp$. Furthermore, in order to have stronger squeezing in $\boldsymbol{k}_\perp$ space, one would expect an efficient nonlinear process which requires

$$|\chi_{nl}| \gg 1 \tag{12}$$

Eqs. (11) and (12) are the essential requirements for the linear and nonlinear susceptibilities to achieve optimal squeezing in a very small spatial area by manipulation of diffraction. This is the key finding from our work. Note that the manipulation of diffraction is operated in momentum space, meaning that it does not depend on the specific spatial profiles of the two quantum fields as long as they are spatially much smaller than the pump fields.

In addition, if one would also like to maximize the spatial squeezing in a large area, then the squeezing angle for small wave components should be in-phase with these critical wave components, i.e., $\phi(\boldsymbol{k}_\perp \simeq 0) \simeq 0$, which leads to

$$\frac{\sqrt{\chi_l^2 - 4\chi_{nl}^2}\zeta_L}{(2m_0 - 1)\pi} \simeq 1 \tag{13}$$

with m_0 being any positive integer. It should be noted that Eq. (13) is not required to achieve extremely localized squeezing which are determined by large wave components.

IV. PHYSICAL IMPLEMENTATION AND RESULTS

To demonstrate how many localized spatial modes can be realized based on our theory, here we explore an example, i.e, the conjugate FWM process to produce MSM squeezing as shown in Fig. 3(a). The interacting Hamiltonian can be written as

$$\begin{aligned}\hat{H}/\hbar = -[&\Delta\hat{\sigma}_{22} + \Delta_{c1}\hat{\sigma}_{33} + (\Delta + \Delta_{c2})\hat{\sigma}_{44} \\ &+ \Omega_{c1}\hat{\sigma}_{31} + \Omega_{c2}\hat{\sigma}_{42} + g_p\hat{a}_p\hat{\sigma}_{32} + g_s\hat{a}_s\hat{\sigma}_{41} + h.c.],\end{aligned} \tag{14}$$

Here we have written $\hat{\sigma}_{ij}(\boldsymbol{r}, t) = \sum_{l=1}^{N} \hat{\sigma}_{ij}^{(l)}(t)\delta(\boldsymbol{r} - \boldsymbol{r}_l)$ as $\hat{\sigma}_{ij}$. g_j is the coupling coefficient for the quantum $\hat{a}_j$, and Ω_{cj} ($j \in \{1, 2\}$) are the two Rabi frequencies of the classical control fields respectively. $\Delta_{c1} = \omega_{c1} - (\omega_3 - \omega_1)$, $\Delta_{c2} = \omega_{c2} - (\omega_4 - \omega_2)$ and $\Delta_p = \omega_p - (\omega_3 - \omega_2)$ are the detunings for the corresponding fields, and $\Delta = \Delta_{c1} - \Delta_p$ is the two-photon detuning for Ω_{c1} and $\hat{a}_p$, and we have $\omega_p + \omega_s = \omega_{c1} + \omega_{c2}$. In order to have spatially homogeneous susceptibilities χ_{jl} for $\hat{a}_p^\dagger$ and $\hat{a}_s$, we have assumed the two classical control fields are spatially much larger than the two quantum fields such that Ω_{c1} and Ω_{c2} can be treated as plane-waves. Assuming the phase-matching condition $k_{c1,z} + k_{c2,z} = k_{p,z} + k_{s,z}$ in z direction, one then obtain Eqs. (1) for $\hat{a}_p^\dagger$ and $\hat{a}_s$.

Experimentally, the MSM squeezing is measured by bichromatic homodyne detection [23, 39] as sketched in Fig. 1(b) where the local oscillator $E_{\text{LO}}(\boldsymbol{r})$ consists of two strong coherent fields whose frequencies match that of the two quantum fields. The squeezing degree is obtained as (see Appendix B)

$$S(\theta, \zeta) = 10 \log_{10} \frac{\iint_{-\infty}^{\infty} d\boldsymbol{k} |B(\boldsymbol{k}_\perp)|^2 G(\boldsymbol{k}_\perp, \theta, \zeta)}{2 \iint_{-\infty}^{\infty} d\boldsymbol{k} |B(\boldsymbol{k}_\perp)|^2} \tag{15}$$

with

$$G(\boldsymbol{k}_\perp, \theta, \zeta) = \sum_{jl} |M_{ij}(\boldsymbol{k}_\perp, \zeta)|^2 - [Q(\boldsymbol{k}_\perp, \zeta) e^{-2i\theta} + c.c] \tag{16}$$

where $i, j \in \{1, 2\}$ and "c.c." denotes complex conjugate. And

$$\begin{aligned}Q(\boldsymbol{k}_\perp, \zeta) = \frac{B^*(-\boldsymbol{k}_\perp)}{B(\boldsymbol{k}_\perp)} [&M_{11}^*(\boldsymbol{k}_\perp, \zeta) M_{21}(\boldsymbol{k}_\perp, \zeta) \\ &+ M_{22}(\boldsymbol{k}_\perp, \zeta) M_{12}^*(\boldsymbol{k}_\perp, \zeta)]\end{aligned} \tag{17}$$

Here we have further assumed that the two coherent fields in $E_{\text{LO}}(\boldsymbol{r})$ have the same momentum spectrum $B(\boldsymbol{k}_\perp)$.

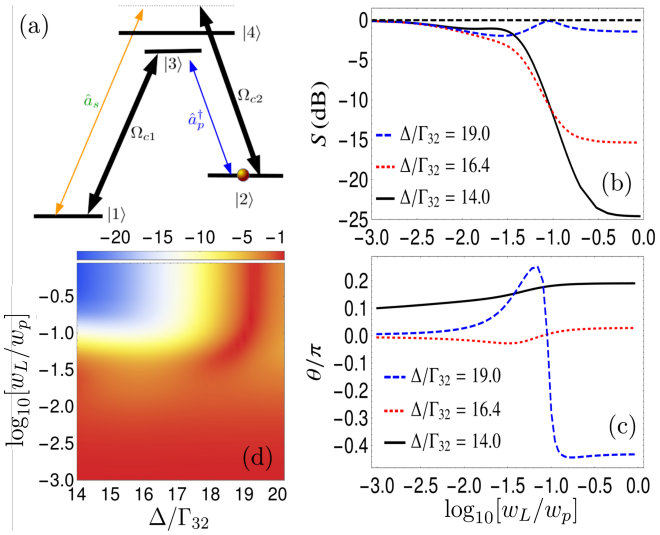

FIG. 3. (Color online) (a) Conjugate FWM process to produce MSM squeezing. The calculated squeezing degree and angle are plotted versus the width of the bichromatic local oscillator w_L for different two photon detuning Δ as shown in (b) and (c) respectively. (d) shows the degree of squeezing as a function of w_L and Δ. Here we have chosen $B(\boldsymbol{\xi}) \propto e^{-k_\perp^2 w_L^2/2}$. Other parameters are: $\Delta_{c1} = 133.3\Gamma_{32}, \omega_{21} = 505.9\Gamma_{32}, \Delta_{c2} = \Delta_{c1} + \omega_{21}, \Omega_{c1} = \Omega_{c2} = 60\Gamma_{32}, n_0 = 4.0 \times 10^{12}$ cm^{-3}, $w_p = 1$ mm, $\Gamma_{32} = 2\pi \times 6$ MHz, $\lambda_p = 795$ nm, and the length of the sample is $L = 1.25$ cm. Parameters are chosen as the same as in the experiment [23] except for Δ.

For a real and symmetric spectrum $B(\boldsymbol{k}_\perp) = B^*(-\boldsymbol{k}_\perp)$, $S(\theta, \zeta)$ reduces to

$$S(\theta,\zeta) = 10\log_{10}\frac{\iint_{-\infty}^{\infty} d\boldsymbol{k}|B(\boldsymbol{k}_\perp)|^2\langle\Delta\hat{X}^2(\boldsymbol{k}_\perp,\zeta,\theta)\rangle}{2\iint_{-\infty}^{\infty} d\boldsymbol{k}|B(\boldsymbol{k}_\perp)|^2} \tag{18}$$

which clearly shows that the spatial squeezing is indeed a weighted summation of squeezing in momentum space which depends on the spatial spectrum of the local oscillator $B(\boldsymbol{k}_\perp)$.

We then calculate the linear and nonlinear susceptibilities and find that $\chi_{nl} > 0$ for all the two-photon detunings Δ considered in Fig. 3 (see Appendix C). Subsequently, the squeezing degree $S(\theta, \zeta)$ defined by Eq. (15) can be obtained. In Fig. 3(b), we have plotted $S(\theta, \zeta)$ as a function of w_L/w_p for different Δ where w_L is the width of the local oscillator. For $\Delta = 16.4\Gamma_{32}$, Eqs. (11a), (12) and (13) are all satisfied such that all spatial wave components contribute constructively to the spatial squeezing. We further notice that the actual phase for the local oscillator remains almost 0 as shown in Fig. 3(c) by the dashed red line, which agrees with our previous analysis presented in Sec. III. The corresponding squeezing S keeps almost unchanged in the range $0.1 < w_L/w_p < 1$, indicating the multimode nature of the spatial squeezing which is insensitive to the mismatch of the transverse

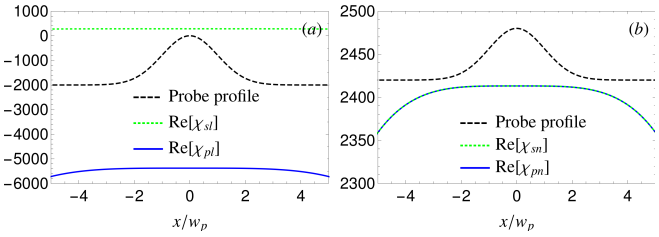

FIG. 4. (Color online) The spatial dependence of the linear and nonlinear dispersions for the probe and signal by applying super-Gaussian control beams with beam waist $w_c = 10w_p$. Here we take the slice for $y = 0$. Note that the dashed black lines only denote the probe profile and are irrelevant to the vertical axis values. Here we choose $\Delta = 16.4\Gamma_{32}$, and other parameters are the same as in the caption of Fig. 3.

modes between the quantum field and the local oscillator. Furthermore, when the local oscillators are displaced by $\boldsymbol{\xi}_0$ in the transverse plane, i.e., $B(\boldsymbol{k}) \to B(\boldsymbol{k})e^{i\boldsymbol{k}\cdot\boldsymbol{\xi}_0}$, it can be seen from Eq. (15) that S does not change. In other words, the spatial squeezing is homogeneous in the probe regime. This is in contrast to the case of single-mode squeezing where the observed squeezing will be degraded considerably for increasing mode mismatch [40–43]. The squeezing decreases from -15.33 dB at $w_L/w_p = 1$ to around -1.51 dB at $w_L/w_p = 0.01$, suggesting localized squeezing at $\sim 10^2\ \mu m^2$ and alternatively 10^4 of spatially squeezed modes in the probe regime which is of an area 1 mm^2.

For comparison, we have plotted S for $\Delta = 14.0\Gamma_{32}$ at which Eqs. (12) and (13) are satisfied but Eq. (11a) is not. In this case, β is real for small $\boldsymbol{k}_\perp$ components such that these components experience exponential growth of squeezing. This leads to the strongest spatial squeezing for $w_L \simeq w_p$ which is determined by small $\boldsymbol{k}_\perp$ components. However, S drops much faster than that in the case of $\Delta = 16.4\Gamma_{32}$ due to the breakdown of Eq. (11a). When increasing Δ to $19.0\Gamma_{32}$, Eq. (11) and (13) are broken and only Eq. (12) is valid, the squeezing is always weaker as compared to the other two cases. An interesting feature here is that the strongest squeezing is obtained at $w_L/w_p = 10^{-1.5}$, this is because in this case the wave components having strongest squeezing locate around $|\boldsymbol{k}_\perp| \sim 1/(10^{1.5}w_p)$.

As $w_L/w_p \to 0.001$, the dominant contributions comes from even larger wave components whose squeezing are negligible, thus the squeezing for all three cases converges to $S \to 0$ which corresponds to the quantum properties of vacuum. We also calculate the squeezing versus Δ and w_L/w_p in Fig. 3(d), in which the squeezing remains almost unchanged for Δ in a wide range $16.0 \leq \Delta/\Gamma_{32} \leq 17.0$, suggesting that it is feasible in realistic experimental settings where the involved laser beams have certain frequency bandwidths.

In the calculation we have made the key approximation that the two control fields can be considered as plane-waves. Practically, this can be satisfied by choosing con-

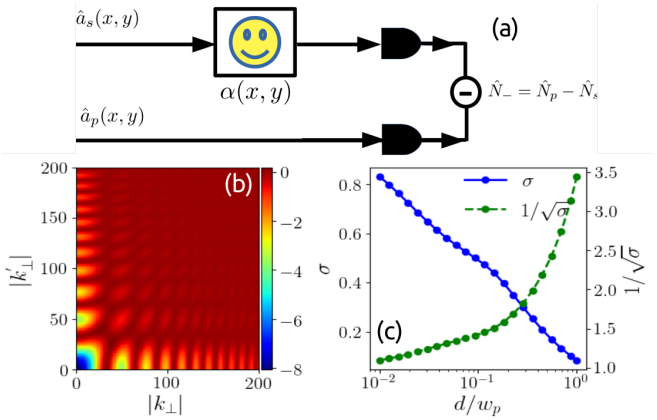

FIG. 5. (Color online) (a) sketch for quantum imaging. (b) $\delta(\boldsymbol{k}_\perp, \boldsymbol{k}_\perp')$ as a function of $k_\perp$ and $k_\perp'$; (c) Noise reduction factor σ and the enhancement factor $E \simeq 1/\sqrt{\sigma}$ as a function of the detector size d. As d increases the squeezing measured at the detector becomes stronger, leading to a better improvement of SNR. Here $\Delta = 16.4\Gamma_{32}$ and other parameters are the same as in the caption of Fig. 3.

trol fields with much larger spatial size as compared to the probe. For example, if taking super-Gaussian spatial profiles for the two control fields as $\Omega_{c1}(\boldsymbol{r}_\perp) = \Omega_{c2}(\boldsymbol{r}_\perp) \propto e^{-\boldsymbol{r}_\perp^4/(2w_c^4)}$ with $w_c = 10w_p$, we find that the relative changes in the direct and cross dispersions are within less than 2% respectively across the probe spatial profile as shown in Fig. 4. Furthermore, since the two strong control fields are far-detuned from the atomic transitions, their propagation dynamics in the medium can be considered as the same in free space, and their spatial profiles remain unchanged during the sample $0 \leq \zeta \leq \zeta_L$. In this respect, the super-Gaussian control beams act as plane-waves in the spatial region of the probe. Note that the absorptions which are not shown in Fig. 4 remain always negligible.

V. APPLICATION IN QUANTUM IMAGING

In order to demonstrate the potential applications of the extremely localized squeezed light obtained here, we further apply our results to image a weakly absorbing object denoted by $\alpha(\boldsymbol{r}_\perp)$ as shown in Fig. 5(a). The output $\hat{a}_s$ is shining on $\alpha(\boldsymbol{r}_\perp)$ and then is measured by the detector of size d^2, meanwhile $\hat{a}_p$ is incident on another detector of the same size; Finally the intensity deference $\delta\hat{N}_- = \hat{N}_p - \hat{N}_s$ is measured (Here $\hat{N}_j = \iint_{-d/2}^{d/2} d\boldsymbol{r}_\perp \hat{a}_j^\dagger(\boldsymbol{r}_\perp)\hat{a}_j(\boldsymbol{r}_\perp)$ for $j \in \{p, s\}$) (see details in Appendix E). For a weakly absorbing object $|\alpha(\boldsymbol{r}_\perp)| \ll 1$, the enhancement in the signal-to-noise ratio (SNR) as compared to the standard quantum limit is given by $E \simeq 1/\sqrt{\sigma}$ where σ is the noise reduction factor [44–49] defined as $\sigma = \langle \delta\hat{N}_-^2 \rangle / \langle \hat{N}_p + \hat{N}_s \rangle$, which can be reduced to

$$\sigma = 1 + \frac{1}{2\pi d^2 N} \iint_{-\infty}^{\infty} d\boldsymbol{k}_\perp d\boldsymbol{k}_\perp' F_d(\boldsymbol{k}_\perp, \boldsymbol{k}_\perp') \delta(\boldsymbol{k}_\perp, \boldsymbol{k}_\perp') \tag{19}$$

with $N = \int_{-\infty}^{\infty} d\boldsymbol{k}_\perp |M_{12}(\boldsymbol{k}_\perp)|^2$ being the total number in either $\hat{a}_p$ or $\hat{a}_s$, and

$$F_d(\boldsymbol{k}_\perp, \boldsymbol{k}_\perp') = d^4 \mathrm{sinc}^2[(k_x - k_x')d/2] \mathrm{sinc}^2[(k_y - k_y')d/2] \tag{20}$$

being the momentum filter defined by the detector size [50], and $\delta(\boldsymbol{k}_\perp, \boldsymbol{k}_\perp') = |M_{12}(\boldsymbol{k}_\perp) M_{12}(\boldsymbol{k}_\perp')|^2 - \mathrm{Re}[M_{11}(\boldsymbol{k}_\perp) M_{12}(\boldsymbol{k}_\perp) M_{11}^*(\boldsymbol{k}_\perp') M_{12}^*(\boldsymbol{k}_\perp')]$ due to the squeezing process (here the ζ dependence is omitted for simplicity). Note here we have neglected the diffraction for $\hat{a}_j(\boldsymbol{r}_\perp)$ during the imaging process, which can be either eliminated by adding lens or reduced by choosing a compact imaging setting. At the optimal condition $\Delta = 16.4\Gamma_{32}$, we plot $\delta(\boldsymbol{k}_\perp, \boldsymbol{k}_\perp')$ as a function of $k_\perp$ and $k_\perp'$ in Fig. 5, which shows a similar oscillation behavior as in Fig. 2 in both directions. For larger d, the filter F_d only covers the small area around $k_\perp = k_\perp'$ where δ is minimized, resulting in maximal E. For decreasing d, F_d takes into account more wave components, and thus E decreases. We found that the enhancement factor E changes from $\sim$ 3.44 for $d/w_p = 1.0$ to $\sim$ 1.1 for $d/w_p = 0.01$ as shown in Fig. 5, suggesting enhanced SNR with high spatial resolution at the near-micrometer regime ($\sim 10\ \mu m$).

VI. SUMMARY

In summary, we have proposed a general and plausible approach to realize extremely localized squeezing in an area of $10^2\ \mu m^2$ with a squeezing degree of -1.51 dB in a probe beam of size 1 mm^2, corresponding to approximately 10^4 squeezed spatial modes. This is achieved by tuning the laser detunings to manipulate the paraxial diffraction such that all the squeezed spatial wave components can contribute constructively to the spatial squeezing based on the analysis of the critical wave components having most significant squeezing. The localized squeezing is further applied to quantum imaging of weakly absorbing object and results in greatly enhanced SNR. Our results may facilitate a number of applications including supersensitive quantum imaging and CV quantum information processing.

L. Zhang is grateful for the fruitful discussions with Tao Peng, Zhenhuan Yi, Fuli Li. We acknowledge the support of Office of Naval Research Grant No. N00014-16-1-3054 and Robert A. Welch Foundation Award No. A1261. We also thank AFOSR Grant No. FA 9550-18-1-0141 for support.

Appendix A: Multi-spatial-mode squeezing

In order to see the multi-spatial-mode nature of squeezing, it is worthwhile to first decompose the input multi-mode quantum field $\hat{a}_j(\boldsymbol{\xi},0)$ into any orthogonal transverse-mode basis

$$\hat{a}_j(\boldsymbol{\xi},0)=\sum_n \phi_n(\boldsymbol{\xi})\hat{a}_{jn}\,, \tag{A.1}$$

with $j\in\{p,s\}$ and $\hat{a}_{jn}$ is the annihilation operator of a photon in the transverse mode $\phi_n(\boldsymbol{\xi})$ at the input plane satisfying $[\hat{a}_m,\hat{a}_n^\dagger]=\delta_{mn}$. The mode functions satisfy the orthogonal and completeness relations $\iint_{-\infty}^{\infty}\phi_m^*(\boldsymbol{\xi})\phi_n(\boldsymbol{\xi})d\boldsymbol{\xi}=\delta_{mn}$ and $\sum_n\phi_n(\boldsymbol{\xi})\phi_n^*(\boldsymbol{\xi}')=\delta(\boldsymbol{\xi}-\boldsymbol{\xi}')$ with δ_{mn} and $\delta(\boldsymbol{\xi}-\boldsymbol{\xi}')$ being the Kronecker and Dirac delta function respectively. From Eq. (A.1) we have $\hat{a}_j(\boldsymbol{k},0)=\sum_n\phi_n(\boldsymbol{k})\hat{a}_{jn}$ with $\phi_n(\boldsymbol{k})=(\sqrt{2\pi})^{-2}\iint_{-\infty}^{\infty}\phi_n(\boldsymbol{\xi})e^{-i\boldsymbol{k}_\perp\cdot\boldsymbol{\xi}}d\boldsymbol{\xi}$. We thus find the solutions for the two fields in position space

$$\hat{a}_p^\dagger(\boldsymbol{\xi},\zeta)=\sum_n a_{pn}^\dagger v_{n,11}^*(\boldsymbol{\xi},\zeta)+\hat{a}_{sn}u_{n,12}(\boldsymbol{\xi},\zeta)\,, \tag{A.2a}$$

$$\hat{a}_s(\boldsymbol{\xi},\zeta)=\sum_n a_{pn}^\dagger v_{n,21}^*(\boldsymbol{\xi},\zeta)+\hat{a}_{sn}u_{n,22}(\boldsymbol{\xi},\zeta)\,, \tag{A.2b}$$

where

$$u_{n,jl}(\boldsymbol{\xi},\zeta)=\iint_{-\infty}^{\infty}\phi_n(\boldsymbol{k})M_{jl}(\boldsymbol{k}_\perp,\zeta)e^{i\boldsymbol{k}_\perp\cdot\boldsymbol{\xi}}d\boldsymbol{k}\,, \tag{A.3a}$$

$$v_{n,jl}^*(\boldsymbol{\xi},\zeta)=\iint_{-\infty}^{\infty}\phi_n^*(-\boldsymbol{k})M_{jl}(\boldsymbol{k}_\perp,\zeta)e^{i\boldsymbol{k}_\perp\cdot\boldsymbol{\xi}}d\boldsymbol{k}\,, \tag{A.3b}$$

where $j,l\in\{1,2\}$. A number of things implied by Eqs. (A.2) and (A.3) are worthy to be stated here. Firstly, the mode functions $u_{n,jl},v_{n,jl}$ at propagation distance ζ_L now depend crucially on the effect of paraxial diffraction included in $M_{jl}(\boldsymbol{k}_\perp,\zeta_L)$. Secondly, the squeezing properties of mode ϕ_n are determined by its spatial frequency spectrum. For the mode function ϕ_n having a narrow spectrum, it will experience stronger squeezing across its modal section; meanwhile, for these modes associated with a broad spectra, the mode functions at ζ_L may be modified significantly by $M_{jl}(\boldsymbol{k}_\perp,\zeta_L)$, and the consequent squeezing will be considerably weakened across its modal section; In short, the number of squeezed spatial modes would critically depend on how we control the system parameters which determine $M_{jl}(\boldsymbol{k}_\perp,\zeta_L)$.

Appendix B: Bichromatic Homodyne Measurement

Experimentally, the squeezing is measured by bichromatic homodyne detection and is defined by the variance of the power difference operator as [23, 39]

$$\hat{P}(\zeta)=i\iint_{-\infty}^{\infty}d\boldsymbol{\xi}[\hat{E}_{sq}(\boldsymbol{\xi},\zeta)\hat{E}_{LO}^\dagger(\boldsymbol{\xi},\zeta)-H.c.] \tag{B.1}$$

where

$$\hat{E}_{sq}=\hat{a}_p(\boldsymbol{\xi},\zeta)+\hat{a}_s(\boldsymbol{\xi},\zeta) \tag{B.2}$$

$$\hat{E}_{LO}=\hat{b}_p(\boldsymbol{\xi},\zeta)+\hat{b}_s(\boldsymbol{\xi},\zeta) \tag{B.3}$$

the local oscillators $\hat{E}_{LO}$ consists of two coherent fields $\hat{b}_p(\boldsymbol{\xi},\zeta)$ and $\hat{b}_s(\boldsymbol{\xi},\zeta)$ whose frequencies are the same as $\hat{a}_p$ and $\hat{a}_s$. Assuming that the coherent fields are much stronger in intensity as compared to the two quantum fields, we then replace $\hat{b}_p$ and $\hat{b}_s$ by $\beta_p b_p(\boldsymbol{\xi})$ and $\beta_s b_s(\boldsymbol{\xi})$ with β_p,β_s and $b_p(\boldsymbol{\xi}),b_s(\boldsymbol{\xi})$ being the amplitude and normalized mode functions respectively. For simplicity, we may assume that $\beta_p=\beta_s=\beta e^{i\theta}$ and $b_p(\boldsymbol{\xi})=b_s(\boldsymbol{\xi})=b(\boldsymbol{\xi})$.

Substituting the expressions for $\hat{E}_s$ and $\hat{E}_{LO}$ to Eq. (B.1) results in

$$\begin{aligned}\hat{P}(\zeta) =& i\beta \iint d\boldsymbol{\xi}\{[\hat{a}_p(\boldsymbol{\xi},\zeta)+\hat{a}_s(\boldsymbol{\xi},\zeta)]b^*(\boldsymbol{\xi})e^{-i\theta} - [\hat{a}_p^\dagger(\boldsymbol{\xi},\zeta)+\hat{a}_s^\dagger(\boldsymbol{\xi},\zeta)]b(\boldsymbol{\xi})e^{i\theta}\} \\ =& i\beta\sum_n \hat{a}_{pn}[v_{n,11}(\zeta)e^{-i\theta} - v_{n,21}(\zeta)e^{i\theta}] + \hat{a}_{pn}^\dagger[v_{n,21}^*(\zeta)e^{-i\theta} - v_{n,11}^*(\zeta)e^{i\theta}] \\ &+ i\beta\sum_n \hat{a}_{sn}[u_{n,22}(\zeta)e^{-i\theta} - v_{n,12}(\zeta)e^{i\theta}] + \hat{a}_{sn}^\dagger[u_{n,12}^*(\zeta)e^{-i\theta} - u_{n,22}^*(\zeta)e^{i\theta}] \end{aligned} \tag{B.4}$$

where

$$v_{n,11}(\zeta) = \iint d\boldsymbol{\xi} v_{n,11}(\boldsymbol{\xi},\zeta)b^*(\boldsymbol{\xi})\,, v_{n,21}^*(\zeta) = \iint d\boldsymbol{\xi} v_{n,21}^*(\boldsymbol{\xi},\zeta)b^*(\boldsymbol{\xi})\,, \tag{B.5a}$$

$$u_{n,12}^*(\zeta) = \iint d\boldsymbol{\xi} u_{n,12}^*(\boldsymbol{\xi},\zeta)b^*(\boldsymbol{\xi})\,, u_{n,22}(\zeta) = \iint d\boldsymbol{\xi} u_{n,22}(\boldsymbol{\xi},\zeta)b^*(\boldsymbol{\xi})\,, \tag{B.5b}$$

We thus find the variance for $\hat{P}$ as

$$\begin{aligned}\langle\Delta\hat{P}^2\rangle =& \langle\hat{P}^2\rangle - \langle\hat{P}\rangle^2 \\ =& 4\beta^2\Big(\sum_n \langle\Delta X_{pn}^2\rangle[v_{n,11}(\zeta)e^{-i\theta} - v_{n,21}(\zeta)e^{i\theta}][v_{n,11}^*(\zeta)e^{i\theta} - v_{n,21}^*(\zeta)e^{-i\theta}] \\ &+ \sum_n \langle\Delta X_{sn}^2\rangle[u_{n,22}(\zeta)e^{-i\theta} - v_{n,12}(\zeta)e^{i\theta}][u_{n,22}^*(\zeta)e^{i\theta} - u_{n,12}^*(\zeta)e^{-i\theta}]\Big)\end{aligned} \tag{B.6}$$

where $\langle\Delta\hat{X}_{jn}^2\rangle = (\langle\hat{a}_{jn}^\dagger\hat{a}_{jn}\rangle + \langle\hat{a}_{jn}\hat{a}_{jn}^\dagger\rangle - 2\langle\hat{a}_{jn}^\dagger\rangle\langle\hat{a}_{jn}\rangle)/4$ with $j\in\{p,s\}$. Suppose now the input quantum probe is in a single-mode coherent state, say, $\langle\hat{a}_{p0}\rangle = \alpha_0$, then we have $\langle\Delta\hat{X}_{pn}^2\rangle = \langle\Delta\hat{X}_{sn}^2\rangle = 1/4$ for all n, which lead us to

$$\begin{aligned}\langle\Delta\hat{P}^2\rangle =& \beta^2\Big(\sum_n |v_{n,11}(\zeta)|^2 + |v_{n,21}(\zeta)|^2 + |u_{n,12}(\zeta)|^2 + |u_{n,22}(\zeta)|^2 \\ &- v_{n,11}(\zeta)v_{n,21}^*(\zeta)e^{-2i\theta} - v_{n,11}^*(\zeta)v_{n,21}(\zeta)e^{2i\theta} - u_{n,22}(\zeta)u_{n,12}^*(\zeta)e^{-2i\theta} - u_{n,22}(\zeta)u_{n,12}^*(\zeta)e^{2i\theta}\Big)\,.\end{aligned} \tag{B.7}$$

Note that

$$\begin{aligned}\sum_n |v_{n,11}(\zeta)|^2 &= \iiiint d\boldsymbol{\xi}d\boldsymbol{\xi}' \sum_n v_{n,11}(\boldsymbol{\xi},\zeta)v_{n,11}^*(\boldsymbol{\xi}',\zeta)f(\boldsymbol{\xi}')f^*(\boldsymbol{\xi}) \\ &= \iiiint d\boldsymbol{\xi}d\boldsymbol{\xi}' \iiiint d\boldsymbol{k}_\perp d\boldsymbol{q}_\perp \sum_n \phi_n(-\boldsymbol{k})M_{11}(\boldsymbol{k}_\perp,\zeta)\phi_n^*(-\boldsymbol{q})M_{11}^*(\boldsymbol{q},\zeta)e^{-i(\boldsymbol{k}_\perp\cdot\boldsymbol{\xi}-\boldsymbol{q}_\perp\cdot\boldsymbol{\xi}')}b(\boldsymbol{\xi}')b^*(\boldsymbol{\xi}) \\ &= \iiiint d\boldsymbol{\xi}d\boldsymbol{\xi}' \iiiint d\boldsymbol{k}_\perp d\boldsymbol{q}_\perp \delta(\boldsymbol{k}-\boldsymbol{q})M_{11}(\boldsymbol{k}_\perp,\zeta)M_{11}^*(\boldsymbol{q},\zeta)e^{-i(\boldsymbol{k}_\perp\cdot\boldsymbol{\xi}-\boldsymbol{q}_\perp\cdot\boldsymbol{\xi}')}b(\boldsymbol{\xi}')b^*(\boldsymbol{\xi}) \\ &= \iiiint d\boldsymbol{\xi}d\boldsymbol{\xi}' \iint d\boldsymbol{k}|M_{11}(\boldsymbol{k}_\perp,\zeta)|^2 e^{-i\boldsymbol{k}_\perp\cdot(\boldsymbol{\xi}-\boldsymbol{\xi}')}b(\boldsymbol{\xi}')b^*(\boldsymbol{\xi}) \\ &= \iint d\boldsymbol{k}_\perp |M_{11}(\boldsymbol{k}_\perp,\zeta)|^2|B(\boldsymbol{k}_\perp)|^2\end{aligned} \tag{B.8}$$

where

$$B(\boldsymbol{k}_\perp) = \iint d\boldsymbol{\xi} b(\boldsymbol{\xi})e^{i\boldsymbol{k}_\perp\cdot\boldsymbol{\xi}} \tag{B.9}$$

is the spatial frequency spectrum of the local oscillator field. Similarly one has

$$\sum_n v_{n,11}(\zeta)v^*_{n,21}(\zeta) = \iint d\boldsymbol{k} M^*_{11}(\boldsymbol{k}_\perp,\zeta)M_{21}(\boldsymbol{k}_\perp,\zeta)B^*(\boldsymbol{k}_\perp)B^*(-\boldsymbol{k}_\perp)\,. \tag{B.10}$$

Thus one find that

$$\begin{aligned}\langle\Delta\hat{P}^2(\theta,\zeta)\rangle =&\langle\hat{P}^2\rangle - \langle\hat{P}\rangle^2\\ =&\beta^2\iint d\boldsymbol{k}_\perp|B(\boldsymbol{k}_\perp)|^2G(\boldsymbol{k}_\perp,\theta,\zeta)\end{aligned} \tag{B.11}$$

with

$$G(\boldsymbol{k}_\perp,\theta,\zeta) = \sum_{jl}|M_{ij}(\boldsymbol{k}_\perp,\zeta)|^2 - \Big\{\frac{B^*(-\boldsymbol{k}_\perp)}{B(\boldsymbol{k}_\perp)}[M^*_{11}(\boldsymbol{k}_\perp,\zeta)M_{21}(\boldsymbol{k}_\perp,\zeta) + M_{22}(\boldsymbol{k}_\perp,\zeta)M^*_{12}(\boldsymbol{k}_\perp,\zeta)]e^{-2i\theta} + c.c.\Big\} \tag{B.12}$$

where $i,j\in\{1,2\}$ and "c.c." denotes complex conjugate.

As in Ref. [23], we now define the spatial squeezing as

$$\begin{aligned}S(\theta,\zeta) =&10\log_{10}\frac{\langle\Delta\hat{P}^2(\theta,\zeta)\rangle}{\langle\Delta\hat{P}^2(\theta,0)\rangle}\\ =&10\log_{10}\frac{\iint_{-\infty}^{\infty}d\boldsymbol{k}|B(\boldsymbol{k}_\perp)|^2G(\boldsymbol{k}_\perp,\theta,\zeta)}{2\iint_{-\infty}^{\infty}d\boldsymbol{k}|B(\boldsymbol{k}_\perp)|^2}\end{aligned} \tag{B.13}$$

Appendix C: Derivation of atomic susceptibilities

As formulated in Ref. [51], The equation of motion for the atomic operators is determined by the following Heisenberg-Langevin equations

$$\left(\frac{d}{dt}+\gamma_{jl}\right)\hat{\sigma}_{jl} = \frac{i}{\hbar}[\hat{H}_1,\hat{\sigma}_{jl}] + \hat{r}_{jl} + \hat{F}_{jl}\,, \tag{C.1}$$

where γ_{jl} are dephasing rates which will be neglected since it is much smaller than the spontaneous decay given by $\hat{r}_{jl}$. $\hat{F}_{jl}$ stand for the Langevin random forces which satisfy

$$\langle\hat{F}_{jl}(\boldsymbol{r},t)\rangle = 0\,, \tag{C.2a}$$

$$\langle\hat{F}^\dagger_{jl}(\boldsymbol{r},t)\hat{F}_{mn}(\boldsymbol{r}',t')\rangle = 2D_{jlmn}\delta(\boldsymbol{r}-\boldsymbol{r}')\delta(t-t')\,. \tag{C.2b}$$

with D_{jlmn} being the diffusion coefficients which can be calculated using the Einstein relationship as shown later.

In the following, we neglect the dephasing terms γ_{jl} which are much smaller that the spontaneous decay in our atom-light interacting system. Then one can obtain the equations of motion for the relevant collective atomic operators

$$\frac{d\hat{\sigma}_{32}}{dt} = i[\Delta_{32}\hat{\sigma}_{32} - \Omega_{c1}\hat{\sigma}_{12} + \Omega_{c2}\hat{\sigma}_{34} + g_p\hat{a}^\dagger_p(\hat{\sigma}_{33}-\hat{\sigma}_{22})] + \hat{F}_{32}\,, \tag{C.3a}$$

$$\frac{d\hat{\sigma}_{12}}{dt} = i[\Delta_{12}\hat{\sigma}_{12} - \Omega_{c1}\hat{\sigma}_{32} + \Omega_{c2}\hat{\sigma}_{14} + g_p\hat{a}^\dagger_p\hat{\sigma}_{13} - g_s\hat{a}_s\hat{\sigma}_{42}] + \hat{F}_{12}\,, \tag{C.3b}$$

$$\frac{d\hat{\sigma}_{34}}{dt} = i[\Delta_{34}\hat{\sigma}_{34} - \Omega_{c1}\hat{\sigma}_{14} + \Omega_{c2}\hat{\sigma}_{32} - g_p\hat{a}^\dagger_p\hat{\sigma}_{24} + g_s\hat{a}_s\hat{\sigma}_{31}] + \hat{F}_{34}\,, \tag{C.3c}$$

$$\frac{d\hat{\sigma}_{14}}{dt} = i[\Delta_{14}\hat{\sigma}_{14} - \Omega_{c1}\hat{\sigma}_{34} + \Omega_{c2}\hat{\sigma}_{12} - g_s\hat{a}_s(\hat{\sigma}_{44}-\hat{\sigma}_{11})] + \hat{F}_{14}\,, \tag{C.3d}$$

where $\Delta_{32}=-\Delta_p+i\Gamma_{32}, \Delta_{12}=\Delta+i\Gamma_{12}, \Delta_{34}=-\Delta_p+\Delta_{c2}+i\Gamma_{34}$ and $\Delta_{14}=\Delta+\Delta_{c2}+i\Gamma_{14}, \Delta=\Delta_{c1}-\Delta_p$, and Γ_{jl} represents the spontaneous decay rates of the corresponding transition respectively. In the following we will choose $\Gamma_{32}=\Gamma_{14}=\Gamma_{34}/2=\Gamma, \Gamma_{12}=0$. Considering the limit that the quantum probe and signal fields are much weak than the control fields, the coherence operators can be considered to be only perturbed. In this case one can then write the atomic operators as

$$\hat{\sigma}_{ij}(\boldsymbol{r},t)=\hat{\sigma}_{ij}^{(0)}+\hat{\sigma}_{ij}^{(1)}(\boldsymbol{r},t)\,, \quad \text{with} \quad \langle\hat{\sigma}_{ij}^{(1)}(\boldsymbol{r},t)\rangle \ll \langle\hat{\sigma}_{ij}^{(0)}\rangle \tag{C.4}$$

where the first constant term in the right hand side is the zeroth-order part when the probe and signal fields are absent, and the second term is the first-order part which is introduced due to the two quantum fields. Since in the zeroth-order limit the quantum effects have been neglected, one can replace the operator $\hat{\sigma}_{ij}^{(0)}$ by a number $\sigma_{ij}^{(0)}$. In typical FWM experiments for squeezing, it is usual that $\hat{a}_p$ and Ω_{c1} is chosen in an EIT structure, and meanwhile, $\hat{a}_s$ and Ω_{c2} forms an ARG configuration. Thus one can find that $\Delta_{c2}\gg\Delta_{c1},\Delta_p,\Omega_{c1},\Omega_{c2}$. Under these conditions, the nonzero zeroth-order matrix elements can be obtained

$$\sigma_{22}^{(0)}=1\,, \quad \sigma_{42}^{(0)}=-\frac{\Omega_{c2}}{\Delta_{c2}+i\Gamma}\,, \quad \sigma_{24}^{(0)}=-\frac{\Omega_{c2}}{\Delta_{c2}-i\Gamma}\,, \tag{C.5}$$

$$\tag{C.6}$$

Eqs. (C.3) are reduced to

$$\frac{d}{dt}\boldsymbol{\sigma}=i\boldsymbol{M}\boldsymbol{\sigma}+i\boldsymbol{v}+\boldsymbol{F}\,, \tag{C.7}$$

where $\boldsymbol{\sigma}=\{\hat{\sigma}_{32}^{(1)},\hat{\sigma}_{12}^{(1)},\hat{\sigma}_{34}^{(1)},\hat{\sigma}_{14}^{(1)}\}^T$, $\boldsymbol{v}=\{g_p\hat{a}_p^\dagger,-g_s\hat{a}_s\sigma_{42}^{(0)},-g_p\hat{a}_p\sigma_{24}^{(0)},0\}^T$, $\boldsymbol{F}=\{\hat{F}_{42},\hat{F}_{12},\hat{F}_{43},\hat{F}_{13}\}^T$, and the matrix $\boldsymbol{M}$ is given by

$$\boldsymbol{M}=\begin{bmatrix}\Delta_{32} & -\Omega_{c1} & \Omega_{c2} & 0\\ -\Omega_{c1} & \Delta_{12} & 0 & \Omega_{c2}\\ \Omega_{c2} & 0 & \Delta_{34} & -\Omega_{c1}\\ 0 & \Omega_{c2} & -\Omega_{c1} & \Delta_{14}\end{bmatrix}. \tag{C.8}$$

The Langevin random force $\hat{F}_{ij}$ is characterized by their diffusion coefficient D_{ijkl} which is defined as

$$\langle\hat{F}_{ij}^\dagger(\boldsymbol{r},t)\hat{F}_{kl}(\boldsymbol{r},t)\rangle=2D_{ijkl}\delta(\boldsymbol{r}-\boldsymbol{r}')\delta(t-t') \tag{C.9}$$

where δ is the Dirac delta function. The diffusion coefficient D_{ijkl} can be calculated using the generalized Einstein relationship [52, 53], then the Langevin force vector $\boldsymbol{F}$ would define the diffusion coefficient matrices as

$$\langle\boldsymbol{F}^\dagger(\boldsymbol{r},t)\boldsymbol{F}(\boldsymbol{r}',t')\rangle=\boldsymbol{D}_1\delta(\boldsymbol{r}-\boldsymbol{r}')\delta(t-t')\,, \tag{C.10a}$$

$$\langle\boldsymbol{F}(\boldsymbol{r},t)\boldsymbol{F}^\dagger(\boldsymbol{r}',t')\rangle=\boldsymbol{D}_2\delta(\boldsymbol{r}-\boldsymbol{r}')\delta(t-t')\,. \tag{C.10b}$$

where $\boldsymbol{D}_1$ and $\boldsymbol{D}_2$ are given by

$$\boldsymbol{D}_1=\begin{bmatrix}0 & 0 & 0 & 0\\ 0 & \frac{2\Gamma\Omega_c^2}{2\Gamma^2+\Delta_{c2}^2+4\Omega_c^2} & 0 & 0\\ 0 & 0 & \frac{2\Gamma\Omega_c^2}{2\Gamma^2+\Delta_{c2}^2+4\Omega_c^2} & -\frac{i2\Gamma^2\Omega_c}{2\Gamma^2+\Delta_{c2}^2+4\Omega_c^2}\\ 0 & 0 & \frac{i2\Gamma^2\Omega_c}{2\Gamma^2+\Delta_{c2}^2+4\Omega_c^2} & \frac{2\Gamma(\Gamma^2+2\Omega_c^2)}{2\Gamma^2+\Delta_{c2}^2+4\Omega_c^2}\end{bmatrix},\quad \boldsymbol{D}_2=\begin{bmatrix}\frac{2\Gamma\left(\Gamma^2+\Delta_{c2}^2+2\Omega_c^2\right)}{2\Gamma^2+\Delta_{c2}^2+4\Omega_c^2} & 0 & \frac{2i\Gamma(\Gamma+i\Delta_{c2})\Omega_c}{2\Gamma^2+\Delta_{c2}^2+4\Omega_c^2} & 0\\ 0 & \frac{2\Gamma\Omega_c^2}{2\Gamma^2+\Delta_{c2}^2+4\Omega_c^2} & 0 & 0\\ -\frac{2i\Gamma(\Gamma-i\Delta_{c2})\Omega_c}{2\Gamma^2+\Delta_{c2}^2+4\Omega_c^2} & 0 & \frac{2\Gamma\Omega_c^2}{2\Gamma^2+\Delta_{c2}^2+4\Omega_c^2} & 0\\ 0 & 0 & 0 & 0\end{bmatrix}. \tag{C.11}$$

In order to obtain the atomic response for the two quantum fields, we need to calculate $\hat{\sigma}_{32}^{(1)}$ and $\hat{\sigma}_{14}^{(1)}$. By performing the Fourier transformation from t to ω in Eq. (C.7) one can then obtain the formal solution as

$$\boldsymbol{\sigma}(\boldsymbol{r},\omega)=i[\boldsymbol{M}+\omega]^{-1}[i\boldsymbol{v}(\boldsymbol{r},\omega)+\boldsymbol{F}(\boldsymbol{r},\omega)] \tag{C.12}$$

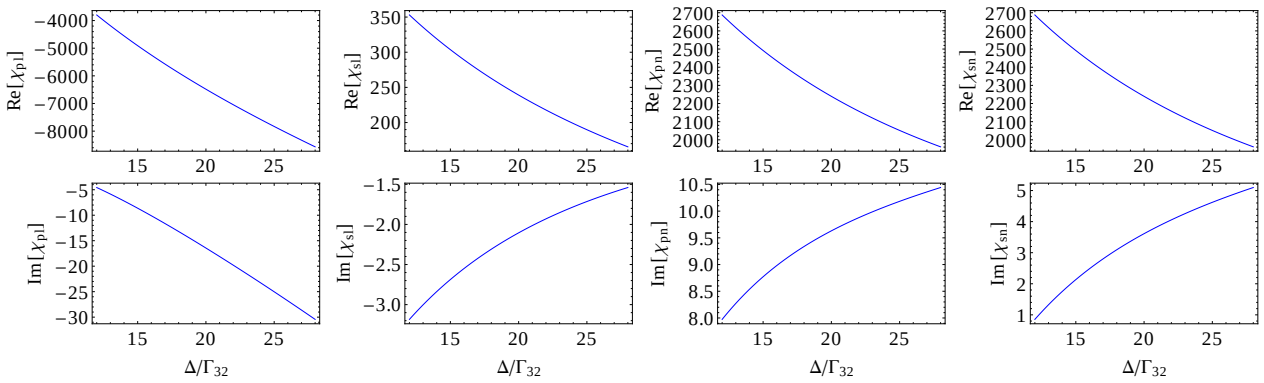

FIG. 6. (Color online) Linear and nonlinear susceptibilities as a function of two-photon detuing Δ. Parameters are the same as in the caption of Fig. 3.

In the following, we consider the continuous-wave limit which means the dependence on ω can be omitted. Then we obtain

$$\hat{\sigma}_{32}^{(1)}(\boldsymbol{r}) = g_p\chi_{pp}\hat{a}_p^\dagger(\boldsymbol{r}) + g_s\chi_{sp}\hat{a}_s(\boldsymbol{r}) + \hat{F}_p(\boldsymbol{r})\,, \tag{C.13a}$$

$$\hat{\sigma}_{14}^{(1)}(\boldsymbol{r}) = g_p\chi_{ps}\hat{a}_p^\dagger(\boldsymbol{r}) + g_s\chi_{ss}\hat{a}_s(\boldsymbol{r}) + \hat{F}_s(\boldsymbol{r})\,, \tag{C.13b}$$

χ_{ij} with $i,j \in \{p,s\}$ describe the atomic properties and can be derived

$$\chi_{pp} = \frac{\Delta_{12}\Delta_{14}\Delta_{34}\sigma_{22}^{(0)} - \Delta_{12}\Delta_{14}\sigma_{24}^{(0)}\Omega_c - \sigma_{22}^{(0)}\Omega_c^2(\Delta_{12}+\Delta_{34})}{\Delta_{12}\Delta_{14}\Delta_{32}\Delta_{34} - \Omega_c^2(\Delta_{12}+\Delta_{34})(\Delta_{14}+\Delta_{32})}\,, \tag{C.14a}$$

$$\chi_{sp} = \frac{\Delta_{14}\Delta_{34}\sigma_{42}^{(0)}\Omega_c}{\Delta_{12}\Delta_{14}\Delta_{32}\Delta_{34} - \Omega_c^2(\Delta_{12}+\Delta_{34})(\Delta_{14}+\Delta_{32})}\,, \tag{C.14b}$$

$$\chi_{ps} = \frac{\Omega_c(\Delta_{12}\Delta_{32}\sigma_{24}^{(0)} - \sigma_{22}^{(0)}\Omega_c(\Delta_{12}+\Delta_{34}))}{\Delta_{12}\Delta_{14}\Delta_{32}\Delta_{34} - \Omega_c^2(\Delta_{12}+\Delta_{34})(\Delta_{14}+\Delta_{32})}\,, \tag{C.14c}$$

$$\chi_{ss} = \frac{-\Delta_{32}\Delta_{34}\sigma_{42}^{(0)}\Omega_c}{\Delta_{12}\Delta_{14}\Delta_{32}\Delta_{34} - \Omega_c^2(\Delta_{12}+\Delta_{34})(\Delta_{14}+\Delta_{32})}\,. \tag{C.14d}$$

thus the susceptibilities can be obtained as $\chi_{pl} = g^2NS_z\chi_{pp}/c$ as defined in the main text, similarly for χ_{sl}, χ_{pn} and χ_{sn}. Their dependences on the two-photon detuning Δ are plotted in Fig. 6.

Appendix D: The effect of optical depth

From our analysis, the spatial squeezing at a small area does not depend on the optical depth. To confirm this, we further calculated the spatial squeezing as a function of w_L/w_p for different length of the atomic sample as shown in Fig. 7. It can be seen indeed that the spatial squeezing at smaller area is almost the same for different length L; At the same time, the squeezing angle is approximately zero, agreeing with our analytical analysis.

Appendix E: High-sensitivity quantum imaging of a weakly absorbing object

In this section, we apply the generated MSM squeezed light to quantum imaging of a weakly absorbing object, and to see if we can obtain higher sensitivity beyond the standard quantum limit. The setup is given in Fig. 8, where the output $\hat{a}_s$ from the squeezing process is shining on a 2D weakly absorbing object represented by $\alpha(x,y)$, which is

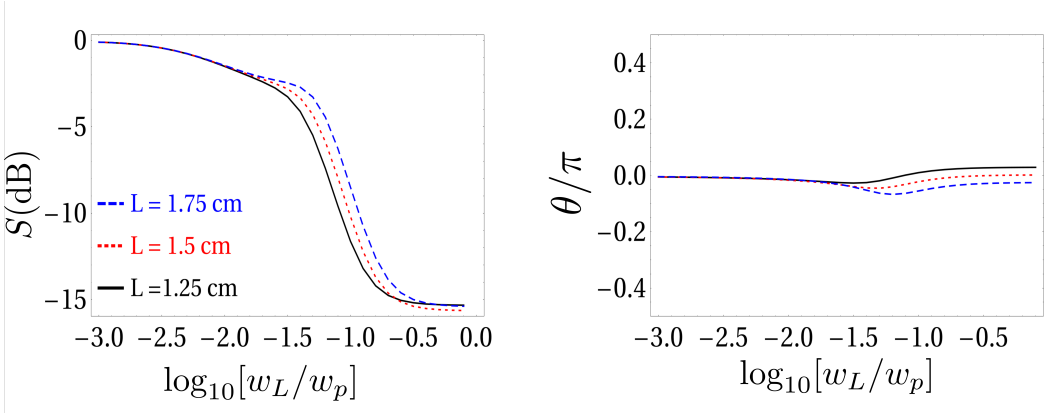

FIG. 7. (Color online) Here we plot the squeezing and the corresponding squeezing angle versus the spatial size of the local oscillator for different length of the atomic sample. Here $\Delta = 16.4\Gamma_{32}$ and other parameters are the same as in the caption of Fig. 3.

further combined with $\hat{a}_p$ in a intensity-difference detector. The singal-to-noise ratio is given by [45]

$$\mathrm{SNR} = \frac{\langle \hat{N}_-^{'} \rangle}{\sqrt{\langle \delta \hat{N}_-^{'2} \rangle}} \tag{E.1}$$

where $\hat{N}_-^{'} = \hat{N}_p - \hat{N}_s^{'}$ being the difference in photon number, $\hat{N}_p$ and $\hat{N}_s^{'}$ are the detected photon numbers in the two fields. After the object, the probe field is changed to

$$\hat{a}_s^{'}(\boldsymbol{r}_\perp) = t(\boldsymbol{r}_\perp)\hat{a}_s(\boldsymbol{r}_\perp) - i\sqrt{1-|t(\boldsymbol{r}_\perp)|^2}\hat{b}(\boldsymbol{r}_\perp) \tag{E.2}$$

where $\alpha(\boldsymbol{r}_\perp) = 1 - |t(\boldsymbol{r}_\perp)|^2$ ($\alpha(\boldsymbol{r}_\perp) \ll 1$) with $t(\boldsymbol{r}_\perp)$ is the transmission coefficient, and $\hat{b}_\perp$ represents the vacuum field. Suppose the input probe field for the squeezing process is vacuum, then the output two fields have the same intensities, i.e., $\langle \hat{a}_p^\dagger \hat{a}_p \rangle = \langle \hat{a}_s^\dagger \hat{a}_s \rangle$. One can find that

$$\hat{N}_-^{'} = \int_A d\boldsymbol{r}_\perp [\hat{a}_p^\dagger(\boldsymbol{r}_\perp)\hat{a}_p(\boldsymbol{r}_\perp) - [1-\alpha(\boldsymbol{r}_\perp)]\hat{a}_s^\dagger(\boldsymbol{r}_\perp)\hat{a}_s(\boldsymbol{r}_\perp) - \alpha(\boldsymbol{r}_\perp)\hat{b}^\dagger\hat{b} + it(\boldsymbol{r}_\perp)\sqrt{1-|t(\boldsymbol{r}_\perp)|^2}(\hat{a}_s^\dagger(\boldsymbol{r}_\perp)\hat{b} - \hat{a}_s(\boldsymbol{r}_\perp)\hat{b}^\dagger)] \,, \tag{E.3}$$

here A stands for the area that is measured and $\boldsymbol{r}_\perp = (x, y)$. In the following, for simplicity we consider α to be constant in the area A. Then we have $\langle \hat{N}_-^{'} \rangle = \alpha N_s$ with $N_j = \langle \hat{N}_j \rangle$ and $\hat{N}_j = \int_A d\boldsymbol{r}_\perp \hat{a}_p^\dagger(\boldsymbol{r}_\perp)\hat{a}_p(\boldsymbol{r}_\perp)$ for $j \in \{p, s\}$. Similarly

$$\langle \hat{N}_-^{'2} \rangle = \langle \hat{N}_p^2 \rangle + (1-\alpha)^2\langle \hat{N}_s^2 \rangle - (1-\alpha)[\langle \hat{N}_p\hat{N}_s \rangle + \langle \hat{N}_s\hat{N}_p \rangle] + \alpha(1-\alpha)N_s \,, \tag{E.4}$$

then we have

$$\begin{aligned} \langle \delta N_-^{'2} \rangle =& (1-\alpha)\langle \delta N_-^2 \rangle + \alpha(\langle \hat{N}_p^2 \rangle - \langle \hat{N}_s^2 \rangle) + \alpha^2\langle \delta \hat{N}_s^2 \rangle + \alpha(1-\alpha)N_s \\ =& (1-\alpha)\langle \delta N_-^2 \rangle + \alpha^2\langle \delta \hat{N}_s^2 \rangle + \alpha(1-\alpha)N_s \,. \end{aligned} \tag{E.5}$$

The signal-to-noise ratio is calculated as

$$\begin{aligned} \mathrm{SNR} =& \frac{\alpha N_s}{\sqrt{(1-\alpha)\langle \delta N_-^2 \rangle + \alpha^2\langle \delta \hat{N}_s^2 \rangle + \alpha(1-\alpha)N_s}} \\ =& \frac{\alpha\sqrt{N_s}}{\sqrt{\alpha^2 Q + 2\sigma(1-\alpha) + \alpha}} \,, \end{aligned} \tag{E.6}$$

where $Q = \langle \delta \hat{N}_s^2 \rangle / \langle \hat{N}_s \rangle - 1$ is the Mandel-Q parameter for the signal field, and

$$\sigma = \frac{\langle \delta \hat{N}_-^2 \rangle}{N_p + N_s} \tag{E.7}$$

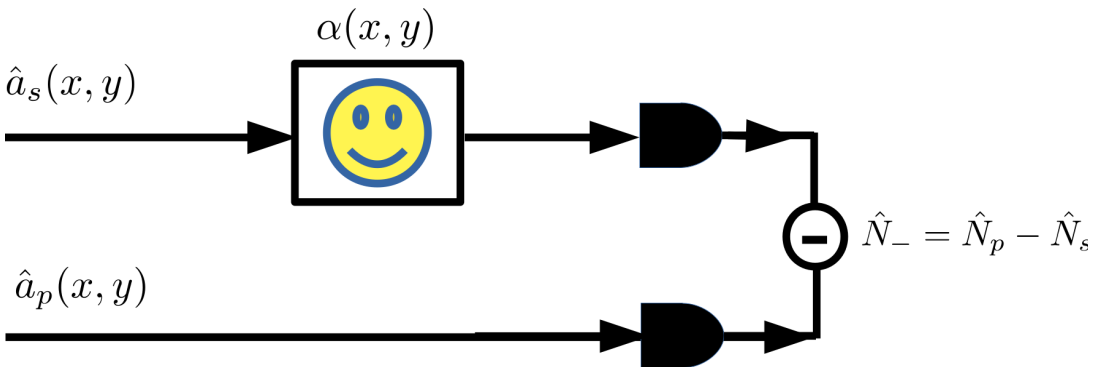

FIG. 8. (Color online) Sketch for quantum imaging with MSM squeezed light.

characterizes the correlation between the two beams. In the case of two coherent beams with equal intensities, we have $Q = 0$ and $\sigma = 1$, and we reach the signal-to-noise ratio at the standard quantum limit as

$$\mathrm{SNR}_{\mathrm{SQL}} = \frac{\alpha\sqrt{N_s}}{2-\alpha}\,. \tag{E.8}$$

We can then define the improvement of the SNR due to squeezed beams with respect to SQL, which is given by

$$E = \frac{\mathrm{SNR}}{\mathrm{SNR}_{\mathrm{SQL}}} = \sqrt{\frac{2-\alpha}{\alpha^2 Q + 2\sigma(1-\alpha)+\alpha}}\,, \tag{E.9}$$

for very weak object $\alpha \ll 1$ we have

$$E \simeq \frac{1}{\sqrt{\sigma}}\,. \tag{E.10}$$

When considering the MSM squeezed beams as we derived in the main text, we have (the ζ dependence for M_{ij} is omitted here for simplicity)

$$N_p = N_s = \frac{1}{(2\pi)^2}\int_A d\boldsymbol{r}_\perp e^{-i(\boldsymbol{k}_\perp^{'}-\boldsymbol{k}_\perp)\cdot\boldsymbol{r}_\perp}\iint_{-\infty}^{\infty} d\boldsymbol{k}_\perp d\boldsymbol{k}_\perp^{'}\langle\hat{a}_s^\dagger(\boldsymbol{k})\hat{a}_s(\boldsymbol{k}_\perp^{'})\rangle = \frac{A}{2\pi}\int_{-\infty}^{\infty} d\boldsymbol{k}_\perp |M_{12}(\boldsymbol{k}_\perp)|^2\,, \tag{E.11}$$

and

$$\begin{aligned}
\langle\delta\hat{N}_-^2\rangle =& \langle\hat{N}_-^2\rangle - \langle\hat{N}_-\rangle^2 \\
=& \frac{2}{(2\pi)^2}\iint_A d\boldsymbol{r}_\perp d\boldsymbol{r}_\perp^{'}\iint d\boldsymbol{k}_\perp d\boldsymbol{k}_\perp^{'}|M_{11}(\boldsymbol{k}_\perp)|^2|M_{12}(\boldsymbol{k}_\perp^{'})|^2 e^{-i(\boldsymbol{k}_\perp-\boldsymbol{k}_\perp^{'})\cdot(\boldsymbol{r}_\perp-\boldsymbol{r}_\perp^{'})} \\
& - \frac{1}{(2\pi)^2}\iint_A d\boldsymbol{r}_\perp d\boldsymbol{r}_\perp^{'}\iint d\boldsymbol{k}_\perp d\boldsymbol{k}_\perp^{'}\big(M_{11}(\boldsymbol{k}_\perp)M_{12}(\boldsymbol{k}_\perp)M_{11}^*(\boldsymbol{k}_\perp^{'})M_{12}^*(\boldsymbol{k}_\perp^{'})e^{-i(\boldsymbol{k}_\perp-\boldsymbol{k}_\perp^{'})\cdot(\boldsymbol{r}_\perp-\boldsymbol{r}_\perp^{'})} + c.c.\big) \qquad \text{(E.12)} \\
=& \frac{2}{(2\pi)^2}\iint_A d\boldsymbol{r}_\perp d\boldsymbol{r}_\perp^{'}\iint d\boldsymbol{k}_\perp d\boldsymbol{k}_\perp^{'}[|M_{11}(\boldsymbol{k}_\perp)|^2|M_{12}(\boldsymbol{k}_\perp^{'})|^2 \\
& - \mathrm{Re}[M_{11}(\boldsymbol{k}_\perp)M_{12}(\boldsymbol{k}_\perp)M_{11}^*(\boldsymbol{k}_\perp^{'})M_{12}^*(\boldsymbol{k}_\perp^{'})]]e^{-i(\boldsymbol{k}_\perp-\boldsymbol{k}_\perp^{'})\cdot(\boldsymbol{r}_\perp-\boldsymbol{r}_\perp^{'})} \qquad \text{(E.13)} \\
=& 2N_p + \frac{2}{(2\pi)^2}\iint_A d\boldsymbol{r}_\perp d\boldsymbol{r}_\perp^{'}\iint d\boldsymbol{k}_\perp d\boldsymbol{k}_\perp^{'}[|M_{12}(\boldsymbol{k}_\perp)|^2|M_{12}(\boldsymbol{k}_\perp^{'})|^2 \\
& - \mathrm{Re}[M_{11}(\boldsymbol{k}_\perp)M_{12}(\boldsymbol{k}_\perp)M_{11}^*(\boldsymbol{k}_\perp^{'})M_{12}^*(\boldsymbol{k}_\perp^{'})]]\cdot e^{-i(\boldsymbol{k}_\perp-\boldsymbol{k}_\perp^{'})\cdot(\boldsymbol{r}_\perp-\boldsymbol{r}_\perp^{'})} \qquad \text{(E.14)} \\
=& 2N_p + \frac{2}{(2\pi)^2}\iint_{-\infty}^{\infty} d\boldsymbol{k}_\perp d\boldsymbol{k}_\perp^{'}F(\boldsymbol{k}_\perp,\boldsymbol{k}_\perp^{'})\big(|M_{12}(\boldsymbol{k}_\perp)|^2|M_{12}(\boldsymbol{k}_\perp^{'})|^2 - \mathrm{Re}[M_{11}(\boldsymbol{k}_\perp)M_{12}(\boldsymbol{k}_\perp)M_{11}^*(\boldsymbol{k}_\perp^{'})M_{12}^*(\boldsymbol{k}_\perp^{'})]\big) \qquad \text{(E.15)}
\end{aligned}$$

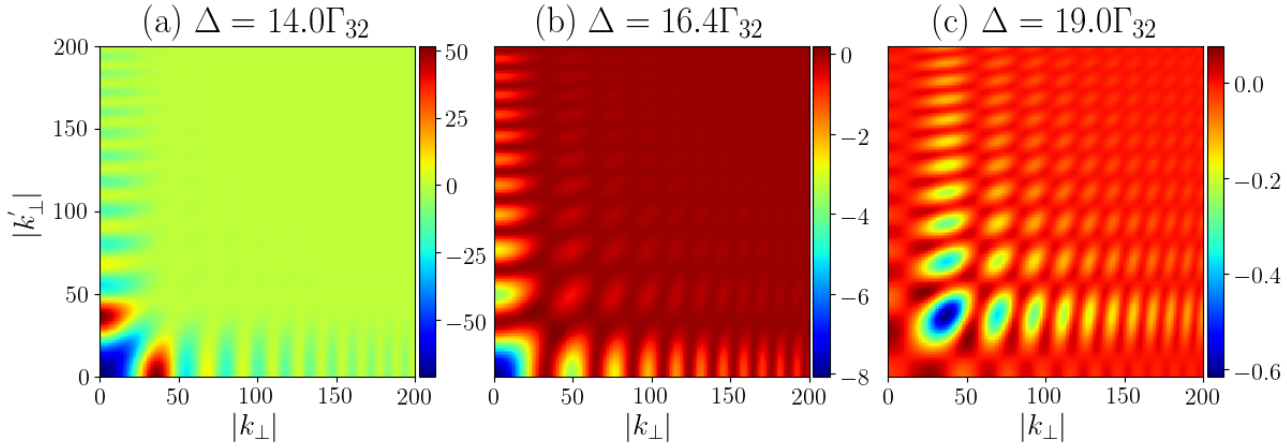

FIG. 9. (Color online) $\delta(\boldsymbol{k}_\perp, \boldsymbol{k}_\perp')$ as a function of $k_\perp$ and $k_\perp'$. Note here the scale for the three cases varies significantly.

where we have applied the relations for $M_{ij}(\boldsymbol{k}_\perp) = M_{ij}(-\boldsymbol{k}_\perp), M_{12}(\boldsymbol{k}_\perp) = M_{21}^*(\boldsymbol{k}_\perp)$ and $M_{11}(\boldsymbol{k}_\perp) = M_{22}^*(\boldsymbol{k}_\perp)$ and $|M_{11}(\boldsymbol{k}_\perp)|^2 - |M_{12}(\boldsymbol{k}_\perp)|^2 = 1$. And $F(\boldsymbol{k}_\perp, \boldsymbol{k}_\perp')$ is the filtering function in momentum space which is defined by the area A. Suppose we define A as a pixel with size d, i.e., $A = d^2$, then we have

$$F(\boldsymbol{k}_\perp, \boldsymbol{k}_\perp') = d^4 \mathrm{sinc}^2[\frac{1}{2}(k_x - k_x')d] \mathrm{sinc}^2[\frac{1}{2}(k_y - k_y')d] \,. \tag{E.16}$$

which agrees well with that derived in Ref. [50]. Finally we have

$$\sigma = \frac{\langle \delta \hat{N}_-^2 \rangle}{N_p + N_s} = 1 + \frac{\iint_{-\infty}^{\infty} d\boldsymbol{k}_\perp d\boldsymbol{k}_\perp' F(\boldsymbol{k}_\perp, \boldsymbol{k}_\perp') \delta(\boldsymbol{k}_\perp, \boldsymbol{k}_\perp')}{2\pi d^2 \int_{-\infty}^{\infty} d\boldsymbol{k}_\perp |M_{12}(\boldsymbol{k}_\perp)|^2} \,. \tag{E.17}$$

with $\delta(\boldsymbol{k}_\perp, \boldsymbol{k}_\perp')$ given by

$$\delta(\boldsymbol{k}_\perp, \boldsymbol{k}_\perp') = |M_{12}(\boldsymbol{k}_\perp)|^2 |M_{12}(\boldsymbol{k}_\perp')|^2 - \mathrm{Re}[M_{11}(\boldsymbol{k}_\perp) M_{12}(\boldsymbol{k}_\perp) M_{11}^*(\boldsymbol{k}_\perp') M_{12}^*(\boldsymbol{k}_\perp')] \tag{E.18}$$

It can be seen from Eq. (E.16) and (E.17) that increasing d leads to smaller σ as the width of the sinc function becomes narrower, and thus a stronger improvement of the SNR. In our system, $\delta(\boldsymbol{k}_\perp, \boldsymbol{k}_\perp')$ only depends on $k_\perp$ and $k_\perp'$ ($k_\perp = \sqrt{k_x^2 + k_y^2}$, the same for $k_\perp'$). We thus plot $\delta(\boldsymbol{k}_\perp, \boldsymbol{k}_\perp')$ as a function of $k_\perp$ and $k_\perp'$ for the three cases as shown in Fig. 9. For $\Delta = 14.0\Gamma_{32}$, since there is exponential squeezing for small $\boldsymbol{k}_\perp$, one might get best σ for large d. However, $\delta(\boldsymbol{k}_\perp, \boldsymbol{k}_\perp')$ soon becomes positive for increasing $\boldsymbol{k}_\perp$, leading to a rapidly decreasing σ. For $\Delta = 16.4\Gamma_{32}$ which corresponds to the case of optimal localized squeezing, δ is always smaller than 0 and leads to a slower decreasing σ when reducing d. Increasing Δ further to $19.0\Gamma_{32}$, σ will be always small as there is only very weakly localized squeezing all the time. The calculated σ and the improvement of the SNR ($\simeq 1/\sqrt{\sigma}$) is plotted in Fig. 5.

[1] C. Fabre and N. Treps, Rev. Mod. Phys. **92**, 035005 (2020).
[2] J. L. O'Brien, A. Furusawa, and J. VuÄ?koviÄ?, Nature Photonics **3**, 687 (2009).
[3] M. I. Kolobov and C. Fabre, Phys. Rev. Lett. **85**, 3789 (2000).
[4] V. Giovannetti, S. Lloyd, and L. Maccone, Science **306**, 1330 (2004).
[5] N. C. Menicucci, S. T. Flammia, H. Zaidi, and O. Pfister, Phys. Rev. A **76**, 010302 (2007).
[6] N. C. Menicucci, S. T. Flammia, and O. Pfister, Phys. Rev. Lett. **101**, 130501 (2008).
[7] N. C. Menicucci, P. van Loock, M. Gu, C. Weedbrook, T. C. Ralph, and M. A. Nielsen, Phys. Rev. Lett. **97**, 110501 (2006).
[8] J. Zhang and S. L. Braunstein, Phys. Rev. A **73**, 032318 (2006).
[9] M. Lassen, V. Delaubert, J. Janousek, K. Wagner, H.-A. Bachor, P. K. Lam, N. Treps, P. Buchhave, C. Fabre,

and C. C. Harb, Phys. Rev. Lett. **98**, 083602 (2007).
[10] M. Gu, C. Weedbrook, N. C. Menicucci, T. C. Ralph, and P. van Loock, Phys. Rev. A **79**, 062318 (2009).
[11] N. C. Menicucci, S. T. Flammia, and P. van Loock, Phys. Rev. A **83**, 042335 (2011).
[12] S. Yokoyama, R. Ukai, S. C. Armstrong, C. Sornphiphatphong, T. Kaji, S. Suzuki, J.-i. Yoshikawa, H. Yonezawa, N. C. Menicucci, and A. Furusawa, Nature Photonics **7**, 982 (2013).
[13] J.-i. Yoshikawa, S. Yokoyama, T. Kaji, C. Sornphiphatphong, Y. Shiozawa, K. Makino, and A. Furusawa, APL Photonics **1**, 060801 (2016).
[14] Petsas, K. I., Gatti, A., Lugiato, L. A., and Fabre, C., Eur. Phys. J. D **22**, 501 (2003).
[15] L. Lopez, S. Gigan, N. Treps, A. Maître, C. Fabre, and A. Gatti, Phys. Rev. A **72**, 013806 (2005).
[16] U. L. Andersen, T. Gehring, C. Marquardt, and G. Leuchs, Physica Scripta **91**, 053001 (2016).
[17] B. Chalopin, F. Scazza, C. Fabre, and N. Treps, Opt. Express **19**, 4405 (2011).
[18] R. E. Slusher, L. W. Hollberg, B. Yurke, J. C. Mertz, and J. F. Valley, Phys. Rev. Lett. **55**, 2409 (1985).
[19] V. Boyer, A. M. Marino, and P. D. Lett, Phys. Rev. Lett. **100**, 143601 (2008).
[20] V. Boyer, A. M. Marino, R. C. Pooser, and P. D. Lett, Science **321**, 544 (2008).
[21] N. Corzo, A. M. Marino, K. M. Jones, and P. D. Lett, Opt. Express **19**, 21358 (2011).
[22] N. V. Corzo, A. M. Marino, K. M. Jones, and P. D. Lett, Phys. Rev. Lett. **109**, 043602 (2012).
[23] C. S. Embrey, M. T. Turnbull, P. G. Petrov, and V. Boyer, Phys. Rev. X **5**, 031004 (2015).
[24] J. Du, L. Cao, K. Zhang, and J. Jing, Applied Physics Letters **110**, 241103 (2017).
[25] I. H. Agha, G. Messin, and P. Grangier, Opt. Express **18**, 4198 (2010).
[26] Z. Qin, L. Cao, H. Wang, A. M. Marino, W. Zhang, and J. Jing, Phys. Rev. Lett. **113**, 023602 (2014).
[27] M. Dowran, A. Kumar, B. J. Lawrie, R. C. Pooser, and A. M. Marino, Optica **5**, 628 (2018).
[28] L. Zhang, G. S. Agarwal, and M. O. Scully, Phys. Rev. Lett. **122**, 083601 (2019).
[29] J. Janousek, K. Wagner, J.-F. Morizur, N. Treps, P. K. Lam, C. C. Harb, and H.-A. Bachor, Nature Photonics **3**, 399 EP (2009).
[30] N. Treps, U. Andersen, B. Buchler, P. K. Lam, A. Maître, H.-A. Bachor, and C. Fabre, Phys. Rev. Lett. **88**, 203601 (2002).
[31] R. C. Pooser and B. Lawrie, Optica **2**, 393 (2015).
[32] M. A. Taylor, J. Janousek, V. Daria, J. Knittel, B. Hage, H.-A. Bachor, and W. P. Bowen, Nature Photonics **7**, 229 EP (2013), article.
[33] M. A. Taylor, J. Janousek, V. Daria, J. Knittel, B. Hage, H.-A. Bachor, and W. P. Bowen, Phys. Rev. X **4**, 011017 (2014).
[34] O. Firstenberg, M. Shuker, N. Davidson, and A. Ron, Phys. Rev. Lett. **102**, 043601 (2009).
[35] L. Zhang and J. Evers, Phys. Rev. A **89**, 013817 (2014).
[36] O. N. Verma, L. Zhang, J. Evers, and T. N. Dey, Phys. Rev. A **88**, 013810 (2013).
[37] D.-S. Ding, Z.-Y. Zhou, and B.-S. Shi, Opt. Lett. **39**, 240 (2014).
[38] L. Zhang, T. N. Dey, and J. Evers, Phys. Rev. A **87**, 043842 (2013).
[39] A. M. Marino, J. C. R. Stroud, V. Wong, R. S. Bennink, and R. W. Boyd, J. Opt. Soc. Am. B **24**, 335 (2007).
[40] L. A. Lugiato and P. Grangier, J. Opt. Soc. Am. B **14**, 225 (1997).
[41] D. Töyrä, D. D. Brown, M. Davis, S. Song, A. Wormald, J. Harms, H. Miao, and A. Freise, Phys. Rev. D **96**, 022006 (2017).
[42] S. Steinlechner, N.-O. Rohweder, M. Korobko, D. Töyrä, A. Freise, and R. Schnabel, Phys. Rev. Lett. **121**, 263602 (2018).
[43] C. Roh, G. Gwak, and Y.-S. Ra, Scientific Reports **11**, 18991 (2021).
[44] O. Jedrkiewicz, Y.-K. Jiang, E. Brambilla, A. Gatti, M. Bache, L. A. Lugiato, and P. Di Trapani, Phys. Rev. Lett. **93**, 243601 (2004).
[45] E. Brambilla, L. Caspani, O. Jedrkiewicz, L. A. Lugiato, and A. Gatti, Phys. Rev. A **77**, 053807 (2008).
[46] J.-L. Blanchet, F. Devaux, L. Furfaro, and E. Lantz, Phys. Rev. Lett. **101**, 233604 (2008).
[47] T. Iskhakov, M. V. Chekhova, and G. Leuchs, Phys. Rev. Lett. **102**, 183602 (2009).
[48] G. Brida, M. Genovese, and I. Ruo Berchera, Nature Photonics **4**, 227 (2010).
[49] A. Meda, E. Losero, N. Samantaray, F. Scafirimuto, S. Pradyumna, A. Avella, I. Ruo-Berchera, and M. Genovese, Journal of Optics **19**, 094002 (2017).
[50] E. Brambilla, A. Gatti, M. Bache, and L. A. Lugiato, Phys. Rev. A **69**, 023802 (2004).
[51] Q. Glorieux, R. Dubessy, S. Guibal, L. Guidoni, J.-P. Likforman, T. Coudreau, and E. Arimondo, Phys. Rev. A **82**, 033819 (2010).
[52] L. Davidovich, Rev. Mod. Phys. **68**, 127 (1996).
[53] R. V. Jones, "Lecture notes on optical physics and quantum electronics," (2000).